Title

Self-sensing concrete enabled by nano-engineered cement-aggregate interfaces

Journal

STRUCTURAL HEALTH MONITORING-AN INTERNATIONAL JOURNAL, 16(3)

ISSN

1475-9217

Authors

Gupta, Sumit
Gonzalez, Jesus G
Loh, Kenneth J

Publication Date

2017

DOI

10.1177/1475921716643867

Peer reviewed

Self-Sensing Concrete Enabled by Nano-Engineered Cement-Aggregate Interfaces

Sumit Gupta[1], Jesus G. Gonzalez[2], and Kenneth J. Loh[1,*]

[1] *Department of Structural Engineering, University of California-San Diego, La Jolla, CA 92093-0085, USA*

[2] *Department of Civil & Environmental Engineering, University of California-Davis, Davis, CA 95616-5294, USA*

** Corresponding author e-mail: kenloh@ucsd.edu*

Abstract

The objective of this study was to design a multifunctional cement composite that could not only bear loads but also possessed electromechanical properties that are sensitive to damage. A mainstream approach is to disperse large quantities of conductive additives in the cement matrix, which can be costly, involve complex procedures, difficult to scale-up, and degrade concrete's inherent mechanical properties. Instead, this research proposes a new method to design multifunctional and self-sensing concrete, which is achieved by altering the cement-aggregate interface using conductive, nano-engineered coatings. Here, a carbon nanotube-based ink solution was sprayed onto the surfaces of aggregates and then dried to form electrically conductive, thin film-coated aggregates. Then, the film-coated aggregates were used as is for casting concrete specimens. It was demonstrated experimentally that this procedure yielded concrete specimens that were not only conductive, but its electrical properties also varied in response to applied physical damage. An electrical impedance tomography (EIT) algorithm was also implemented and used for estimating their spatial resistivity distributions. Since the electrical properties at every location of the film-enhanced concrete were sensitive to damage, EIT was able to produce electrical resistivity maps that indicated the locations and severities of damage. Multiple concrete cylinder, plate, and beam specimens were cast and tested for validating the self-sensing properties of film-enhanced concrete and the spatial damage detection capabilities of the EIT algorithm.

Keywords

Carbon nanotube, cement composite, damage localization, electrical impedance tomography, interface, self-sensing, thin film.

Introduction

Research on multifunctional cementitious composites has garnered much interest due to their potential widespread applications for civil infrastructure health monitoring in lieu of using conventional sensors such as accelerometers, strain gages, and fiber optics, among others. A mainstream approach to design these cementitious composites is by incorporating conductive additives as part of the cement matrix and during casting.[1,2] In fact, the development of multifunctional cementitious composites using conductive fibers can be traced back to the early 1990s. These fibers were sought out as a way to simultaneously improve both the mechanical and electrical performance of concrete.

For instance, Banthia and Sheng[3] demonstrated that, by using mono and hybrid fiber mixtures of steel and carbon fibers in large quantities (*i.e.*, anywhere from 1 to 5 *wt.*%), significant improvements in flexural strength and toughness were achieved. Further research by Banthia *et al*.[4] sought to relate changes in the composites' resistivity due to the inclusion of these conductive fibers. While large amounts of conductive fibers increased conductivity, their size and distribution within the composite had large effects on conductivity change. Ding *et al*.[5] and Cheng and Chung[6] also used steel and carbon fibers to alter the cementitious composites' electrical properties for sensing applied loads. In particular, Ding *et al.*[5] was able to relate increases in the fractional change in resistance due to increased crack length. Cheng and Chung[6] performed similar tests and showed that carbon fiber-based specimens exhibited changes in resistance that followed an applied load pattern to confirm sensing capabilities; permanent changes in the specimens' resistance were attributed to irreversible damage. It was also shown that sensing repeatability and sensitivity could be improved by treating the carbon fibers with ozone.[7] Despite these aforementioned advances, the use of these conductive fibers as additives in the cement matrix are limited by how effectively they can be dispersed. Poor dispersion prevents fibers from forming a percolated and conductive network necessary to enable damage sensitivity. Simply increasing fiber concentrations to overcome this issue is not practical, since high costs would make production of the composites impractical, not to mention the adverse effects on the workability of the mix.

More recently, conductive nanomaterials have been used for developing multifunctional cementitious composites with properties that have surpassed those aforementioned fiber-based cementitious composites. The benefits of using nanomaterials are to leverage their impressive intrinsic material properties, large surface areas for interacting with the cement matrix, and the potential of using lower concentrations.[8] Carbon nanotubes (CNT) were at the forefront of this movement, due to their exceptional mechanical and electrical properties.[9,10] Unfortunately, nanomaterials such as CNTs have a strong tendency to agglomerate, thereby making it difficult to take advantage of their unique properties. Thus, various dispersion techniques are commonly used, such as by using surfactants and ultrasonication for dispersing CNTs in aqueous solutions. Dispersed CNT solutions can then be directly added to the concrete mix during casting. For example, Yu and Kwon[11] compared the dispersion of CNTs using an acid treatment to form surface carboxylic groups versus using a surfactant. Both were found to be effective in achieving adequate CNT suspensions, but cementitious composites cast using the surfactant-dispersed CNTs exhibited smaller signal-to-noise ratios, while the acid-treated CNTs exhibited greater piezoresistivity. Other surfactants, such as poly(sodium 4-styrenesulfonate)[12]

and octyl-phenol-exthoxylate[13], were also tested, as well as other nanomaterials such as carbon black[14], graphite[15], and nickel powder.[16] It should be mentioned that hybrid mixtures were also investigated (*e.g.*, using both carbon black and carbon fibers).[17] Although conductive fibers and nanomaterials have been shown to enhance both the mechanical and electrical properties of cementitious composites, they still suffer from some challenges (*e.g.*, high costs, high concentrations, dispersion, and scalability issues, to name a few) that have limited their real-world use. Most studies to date have been confined to the laboratory or small-scale applications in real-world settings.

In this study, a new method for efficiently incorporating CNTs to form multifunctional cementitious composites that preserved the mechanical properties of conventional concrete while providing enhanced electromechanical sensitivity to damage was developed. Rather than using brute-force techniques for dispersing nanomaterials in the cement matrix, the approach was to modify the cement matrix-aggregate interface or interfacial transition zones with CNT-based thin films. These films were developed in a previous study by Mortensen *et al*.[18] and contained dispersed CNTs in a latex matrix, which can be fabricated by airbrushing or spraying CNT-latex inks onto any surface. More specifically, multi-walled carbon nanotube (MWNT)-latex films were directly coated onto the surfaces of fine and coarse aggregates. Film-coated aggregates were then used as is for casting concrete specimens, following typical mix designs and casting procedures. In doing so, the embedded thin films that were uniformly distributed within the cementitious composite provided mechanisms for which electrical current could flow through the bulk material. Disruptions to the material's ability to conduct electrical current due to damage would then cause detectable changes in the bulk material's conductivity. Furthermore, this study also employed an electrical impedance tomography (EIT) algorithm for estimating the cementitious composites' spatial conductivity (or resistivity) distributions. Since electrical conductivity at every location in the composite is sensitive to damage, the EIT conductivity maps allow one to visualize the severities, locations, and physical attributes of damage occurring in the system.

This paper begins with a detailed discussion of EIT and its formulation. The concrete mix design and casting procedures are then presented, as well as a short discussion on how MWNT-latex thin films were prepared and deposited onto fine and coarse aggregates. A series of experiments was performed for assessing the cementitious composites' mechanical properties and to validate their spatial damage detection capabilities using EIT. Finally, a discussion of the results is presented, followed by a brief conclusions section.

EIT Background

Electrical impedance tomography is a soft-field tomography technique that seeks to estimate the conductivity distribution of a conductive body using only electrical excitations and corresponding voltage measurements obtained along the body's boundaries.[19] In fact, EIT was successfully used in biology and biomedical fields of study for obtaining electrical images and for revealing anomalies inside the bodies of humans or animals. For example, the rate of gastric emptying was studied with the aid of EIT by Barber *et al.*[20], in which the spatial resistivity distribution of the stomach was evaluated as a function of time so as to obtain an emptying curve. More applications of EIT on gastric imaging can be found in Dijkstra *et al.*[21] and Smallwood *et al.*[22] Other applications of EIT include the assessment of pulmonary and cardiac parameters[23-26], detection of internal intraventricular hemorrhages in newborns [27], and to diagnose intrathoracic fluid volume[28], among others.

Although EIT has been successfully demonstrated in bio-related disciplines, its applications for structural health monitoring (SHM) remain fairly new and require further development. Early work by Loh *et al.*[29] showed that EIT can be coupled with layer-by-layer CNT-based thin films for monitoring spatially distributed strain and impact damage on metallic structural components. Loyola *et al.*[30,31] incorporated spray-coated MWNT-latex thin films and embedded them in glass-fiber reinforced polymer (GFRP) composites for damage detection. Zhang *et al.*[32] demonstrated the SHM potential in GFRP, whose glass fibers were laminated with an epoxy resin containing carbon black. This process enhanced the electrical conductivity of GFRP, and damage was detected within the composite by calculating the in-plane and through-thickness conductivity changes with the aid of electrical resistance tomography. Tallman *et al.*[33] also showed that epoxy composites can be filled with carbon nano-fibers (CNF) for encoding self-sensing characteristics. Local changes in conductivity due to damage in CNF-enhanced epoxy composites was also captured using EIT. Instead of CNT- or CNF-based materials, Hallaji *et al.*[34] employed colloidal silver paints applied directly onto concrete surfaces, and localized changes in electrical conductivity due to cracking or surface damage was subsequently detected by EIT analysis. On the other hand, Hou *et al.*[35,36] applied EIT for directly mapping the spatial conductivity distributions of engineered cementitious composites and detected regions in which micro-cracking occurred during load testing. More recently, Gupta *et al.*[37] used the same approach in this study but deposited MWNT-latex thin films onto sand for casting smart mortar specimens with nano-engineered cement-sand interfaces. Their results validated the piezoresistive properties of mortar specimens, and EIT was able to identify the location of damage

created by drilled holes. Despite this, the influence of the coating on bulk material mechanical properties and spatial damage detection in concrete has not been demonstrated and is the primary focus of this work.

In short, EIT consists of the forward and inverse problems. The forward problem describes the calculation of the boundary voltage distribution given a known boundary electrical excitation and knowledge of the spatial conductivity or resistivity distribution of the body. However, for SHM purposes, EIT requires the inverse problem to be solved. The corresponding boundary voltages can be obtained experimentally for any applied boundary electrical current excitation; the objective is to solve this ill-posed inverse problem and to estimate the spatial distribution of electrical properties. The forward and inverse problems are described in detail in the following sections.

Forward Problem

As mentioned earlier, the forward problem uses *a priori* information of spatial conductivity distribution (σ) of a conductive body (Ω) and a known boundary electrical current excitation for computing the corresponding boundary voltage response. Flow of electric charge through Ω can be explained by Laplace's equation, as shown in equation (1), which correlates the conductivity distribution with the electric potential distribution (u) in absence of any current source or sink inside Ω.

$$\nabla \cdot (\sigma \nabla u) = 0 \tag{1}$$

This second-order partial differential equation needs to be solved with appropriate boundary conditions to get the boundary voltage distribution. Several numerical methods have been implemented for solving this elliptic partial differential equation. Sherina *et al.*[38] used the finite volume method for an unstructured grid. Lazarovitch *et al.*[39] employed the finite difference method for solving equation (1). Besides these, the finite element method remains to be one of the most widely used numerical tools for obtaining robust and accurate solutions.[19,40-42]

In the theoretical formulation of the EIT forward problem, applied electrical current and boundary voltage distributions are taken into account as continuous functions along the entire boundary. Previous research showed that it is not only impractical to represent boundary excitations and voltage measurements in the continuum sense, but the resistivity values are also overestimated using this approach.[43] In this study, discrete boundary electrodes are employed and distributed throughout the entire boundary (Γ) of Ω, and electrical current and voltage are only applied and measured,

respectively, at these electrodes. Typically, the complete electrode model (*i.e.*, equations 2 to 4) is used to incorporate the proper boundary conditions for the EIT finite element model,[40,42] which allows one to model the shunting effect and contact impedance between the electrode and the body without any overestimation.

$$\int_{e_l} \sigma \nabla u \cdot n = I_l \text{ on } \Gamma_1 \tag{2}$$

$$\sigma \nabla u \cdot n = 0 \text{ on } \Gamma_2 \tag{3}$$

Here, e_l is the area of l^{th} electrode, and I_l is the current in the l^{th} electrode on the surface as defined by a normal vector, n, perpendicular to that surface. Γ_1 is the region of the boundary associated with all the electrodes, and Γ_2 is the remainder of the boundary. Contact impedance between electrodes and the body is taken into account in equation (4), which is used to calculate the boundary electrode voltages:

$$u + z_l \sigma \nabla u \cdot n = V_l \text{ on } \Gamma_1 \tag{4}$$

where z_l is the contact impedance at the l^{th} electrode, and V_l is the measured voltage at the l^{th} electrode.

The subsequent weak-form of the EIT problem has been derived by multiplying equation (1) with a sufficiently smooth arbitrary test function (v) and integrating over the entire Ω:

$$\int_{\Omega} v \nabla \cdot (\sigma \nabla u) = 0 \tag{5}$$

Integrating equation (5) using integration by parts results in the boundary expression as follows:

$$\int_{\Omega} \sigma \nabla u \cdot \nabla v dx^2 = \int_{\Gamma} \sigma \nabla u \cdot n v dx \tag{6}$$

The right-hand-side of equation (6) can be rewritten as equation (7).

$$\int_{\Omega} \sigma \nabla u \cdot \nabla v dx^2 = \int_{\Gamma_1} \sigma \nabla u \cdot n v dx + \int_{\Gamma_2} \sigma \nabla u \cdot n v dx \tag{7}$$

Substituting equations (3) and (4) into equation (7) yields:

$$\int_{\Omega} \sigma \nabla u \cdot \nabla v dx^2 + \sum_{l=1}^{L} \frac{1}{z_l} \int_{e_l} u v dx = \sum_{l=1}^{L} \frac{1}{z_l} \int_{e_l} V_l v dx \tag{8}$$

where L is the total number of boundary electrodes. According to finite element theory, the electric potential, u, is approximated (u^h) as a linear combination of nodal voltage (u_i) and the nodal shape function (ϕ_i).

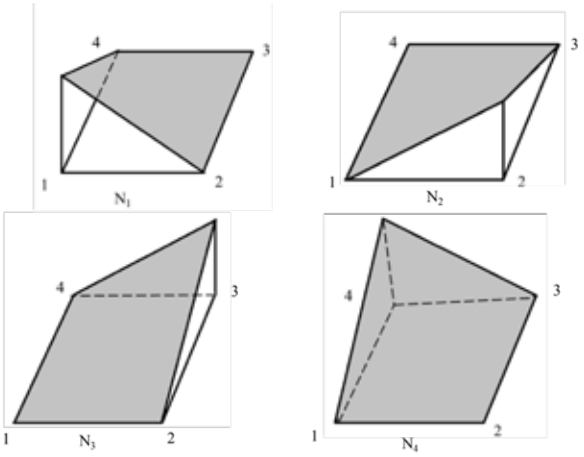

Figure 1. Four shape functions and their values at each node of a four-node quadrilateral element are shown. The values of the shape function corresponding to the i^{th} node is 1 at that node and 0 at all other nodes in accordance with the compacted support property.

$$u^h = \sum_{i=1}^{n} u_i \phi_i \tag{9}$$

Four-node bi-linear quadrilateral elements can be used to discretize the entire domain, and the properties of the shape functions are shown in Figure 1. All the calculations have been carried out in the regular bi-unit square domain and thereafter transferred into the real domain using iso-parametric formulation.[44,45]

Galerkin's approximation states that the test function can be chosen to be the same as the nodal shape function, which turns equation (8) to the following form:

$$\sum_{i=1}^{n} u_i \left(u_i \nabla \phi_i \cdot \nabla \phi_j dx^2 + \sum_{l=1}^{L} \frac{1}{z_l} \int_{e_l} \phi_i \phi_j dx \right) = \sum_{i=1}^{n} \frac{1}{z_l} \int_{e_l} V_l \phi_j dx \tag{10}$$

The boundary condition mentioned in equation (2), when applied on u^h and combined with equation (4), results into L number of additional linear equations:

$$\frac{1}{z_l} V_l \mid e_l \mid - \sum_{i=1}^{n} \left(\int_{e_l} \frac{1}{z_l} \phi_i dx \right) u_i = I_l \tag{11}$$

Assembling all these expressions finally leads into a matrix equation of the following form:

$$Au = I \tag{12}$$

where A, u, and I are the global conductivity matrix, vector containing the nodal values of potential distributions, and generalized current vector, respectively. A is composed of four elementary matrices A_M, A_Z, A_V, and A_D:

$$A = \begin{bmatrix} A_M + A_Z & A_V \\ A_V^T & A_D \end{bmatrix} \tag{13}$$

where,

$$A_M(i,j) = \iint_{\Omega} \sigma \nabla \phi_i \cdot \nabla \phi_j dx^2 \tag{14}$$

$$A_Z(i,j) = \sum_{l=1}^{L} \frac{1}{z_l} \int_{e_l} \phi_i \phi_j dx^2 \tag{15}$$

$$A_V(i,l) = -\frac{1}{z_l} \int_{e_l} \phi_i dx \; (i=1{:}n \text{ and } l=1{:}L) \tag{16}$$

$$A_D(k,l) = \frac{1}{z_l} |\, e_l \,| \text{ (for } l=k) \tag{17a}$$

$$A_D(k,l) = 0 \text{ (for } l \neq k) \tag{17b}$$

Inverse Problem

While the solution of the forward problem predicts the boundary voltage data when the conductivity distribution of the body is known, the inverse problem seeks to estimate conductivity distribution using measured boundary voltages. The EIT inverse problem is non-linear by nature as the number of unknown terms (*i.e.*, conductivity value at each voxel) is greater than the number of known terms (boundary voltages). The inverse problem is also ill-posed, since a large perturbation in conductivity distribution often results in very small changes in boundary responses. An iterative Gauss-Newton algorithm has been used for solving this non-linear and ill-posed inverse problem. The iteration process starts with an initial assumption of conductivity distribution, and boundary voltages (V_c) can be calculated using a given boundary electrical excitation and then by solving the forward problem with a finite element model of the body. The measured boundary voltages (V_m) are then used to calculate the error vector (e) by evaluating the difference between V_m and V_c, as described in equation (18):

$$e = (V_m - V_c) \tag{18}$$

A new conductivity distribution is then predicted by solving the inverse problem upon which the aforementioned procedure repeats, and the boundary voltage is calculated again by solving the forward problem. This procedure is repeated as long as the error ratio (ϵ) of the norm of error vector and the norm of the measured boundary voltage remains greater than a preset error threshold (0.05%):

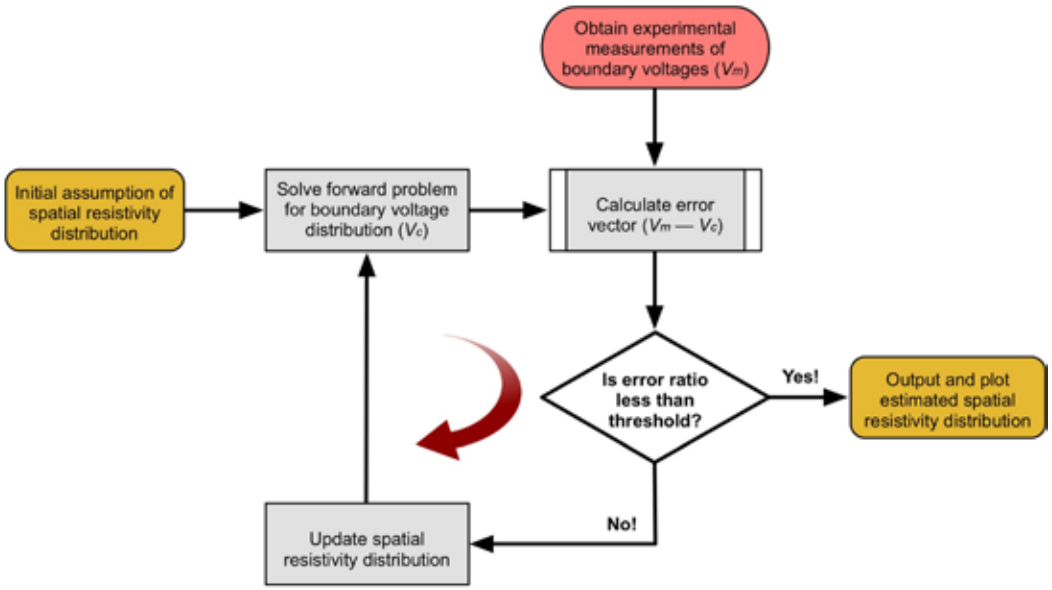

Figure 2. The flow chart illustrates the forward and inverse problems of the EIT algorithm.

$$\varepsilon = \frac{\| e \|^2}{\| V_m \|^2} \leq 0.05\% \tag{19}$$

It should be recognized that regularization is necessary since EIT is an ill-posed inverse problem and to ensure the smooth and fast convergence of the algorithm. The Tikhonov regularization method was implemented for calculating the regularization matrix and regularization parameter in this work. A flow diagram of the entire EIT forward and inverse problems is illustrated in Figure 2.

Experimental Details

Cementitious Composite Mix Design

The concrete mix design employed in this study followed the Federal Aviation Administration (FAA) runway rigid pavement guidelines[46]. Here, type I/II Portland cement and 25 *wt.%* (of total cementitious material) type F ground granulated blast furnace slag (GGBFS) were used. The fine aggregates were crushed granite with a density of 2.71 g/cm^3 and a minimum sieve size of 0.149 mm, and a 2:1 sand-to-cement ratio was employed. The large aggregates were 19 mm (0.75 in) river rock with a specific gravity of 2.7, and an aggregate-to-cement ratio of 3:1 was used. Selection of both fine and large aggregates conformed to the FAA guidelines on gradation[46]. All of the aggregates were cleaned and oven-dried at 80 °C for 24 h and then allowed to cool to room temperature for 1 h, before MWNT-latex thin films were deposited on their surfaces, which will be explained in the next section. Water-to-cement (w/c)

(a) (b)

Figure 3. MWNT-latex inks are airbrushed to form thin films on (a) large or coarse aggregates and (b) sand.

ratios ranging from 0.42 to 0.44 were used along with an Advacast superplasticizer (SPL). A range of w/c ratios was used due to different casting environments and ambient temperatures, but the SPL concentration was maintained at 3.5 mL/kg for all the specimens.

Film Fabrication

As was stated before, MWNT-based thin films were deposited onto fine (sand) and coarse or large aggregates before casting for modifying the cement-aggregate interface of concrete. The procedure for film fabrication was presented in detail in a previous study[18] but is briefly summarized here. First, MWNTs were dispersed in 2 *wt.*% poly(sodium 4-styrensulfonate) (PSS) aqueous solutions. Dispersion was achieved by subjecting the solutions to ultrasonication. Second, Kynar Aquatec latex was added to obtain the final MWNT-latex ink.[18,47] In this work, film deposition was performed manually by holding a Paasche airbrush 30 cm (12 in) above the aggregate surface and then spraying the MWNT-latex ink by hand, as shown in Figure 3. Once a uniform film was deposited onto the surfaces of aggregates, the film-coated aggregates were manually mixed with a plastic spatula to expose uncoated aggregate surfaces. Airbrushing was then repeated. To obtain uniform coatings, sand required twice as much MWNT-latex ink than the large aggregates; a total of six coatings were applied for sand and three for large aggregates. After spraying was finished, the treated aggregates were air-dried at room temperature for 30 min and then placed in a vacuum oven set to 80 °C for 30 min. The film-coated sand and aggregates were allowed to cool to room temperature prior to being used for concrete casting. Figure 4 shows a scanning electron microscope (SEM) image of an MWNT-latex thin film, which in this case was deposited onto a sand particle.

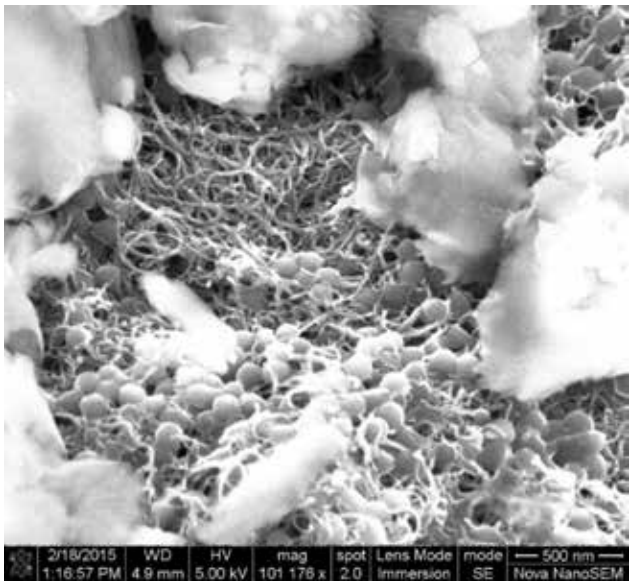

Figure 4. An SEM image of a thin film deposited on a sand particle shows that carbon nanotubes (thin, white lines) and latex spherical particles are uniformly deposited.

Concrete Casting Procedure

Due to smaller volumes of material, concrete plate specimens were cast using a small-scale Hobart N-50 mixer. First, cementitious material and water were added to the mixing bowl. The mixer speed was set to 60 rpm and was run for 30 s to evenly hydrate the cementitious mixture. Second, after initial mixing, SPL was added, and the contents were mixed for another 2 min. During this time, sand (either pristine or coated with thin films), was added to the mixer in equal proportions every 30 s. Once all of the sand had been incorporated, the mixer was stopped, and the bowl was removed so that the large aggregates could be added. The large aggregates were poured into the bowl in small proportions, and a garden trowel was used to manually mix the contents for 30 s before more aggregates were added. This process was repeated until an even and workable mixture was obtained.

Plate specimens were cast using two custom poly(vinyl chloride) (PVC) molds that measured 125×350×18 mm^3. The molds had their seams sealed with white petrolatum and their surfaces oiled with WD-40 as a releasing agent before the concrete mix was poured into the molds. The objective was to use each large plate to obtain three individual smaller plate specimens that each measured 80×80×18 mm^3. Since these concrete specimens would be subjected to spatial damage detection tests using EIT, custom Balsa wood formworks for placement of boundary electrodes were also fabricated and used during casting. The formwork held 24 equally spaced copper mesh electrodes arranged in a

6×6 square pattern, and the formwork was placed on top of the PVC concrete molds so that the electrodes could be embedded and casted with the specimens. Upon pouring the mix into the molds, a 3.2 mm (0.125 in) steel rod was employed for tamping the concrete for 1 min, and further compaction was performed using a shake table operated at 5 Hz for 1 min. Finally, the top of the molds was covered with clear plastic wrap to avoid surface cracking due to uneven curing and drying. They were stored at room temperature for 24 h before being demolded and placed in a curing solution for 14 days.

Cylinder and beam specimens were also cast for compressive and flexural strength tests, respectively, using the same mix design. For these specimens, a MultiQuip large capacity cement mixer was employed for casting. The casting procedure was similar, in which the dry ingredients (cement and aggregates) were mixed for 30 s before water and SPL were added. The mixture was then mixed for 5 min. For the cylinder specimens, 10 mm-diameter (4 in) and 20 mm-tall (8 in) cylinder molds were used. These cylinders were filled with two lifts of concrete, where each lift was tamped 25 times using a 14 mm (0.55 in) steel rod.[48] Cylinders were capped and placed in a water bath for three days before being demolding, followed by a curing bath for 28 days. On the other hand, beam specimens were cast using a custom 15×15×46 mm^3 (6×6×18 in^3) PVC molds. The interior of the molds was coated with WD-40 as a releasing agent and its seams sealed with white petrolatum. Two walls of the mold also had 6.4 mm (0.25 in) holes drilled to form an 8×8 square pattern. Copper mesh electrodes were inserted into these holes during casting (and holes were filled with paraffin wax) to form the boundary electrodes needed for future EIT testing. Casting was done by adding the mix in three lifts, and tamping was performed after each pour.[48] After filling the mold, additional compaction was achieved using a concrete vibrator. Beam specimens were then covered in clear plastic wrap and stored at room temperature for 48 h before being demolded and placed in a curing solution for 28 days. In total, four unique sets of cylinder and beam sample sets were cast. The four types were the sample sets that used film-treated sand, film-treated large aggregates, both film-treated sand and large aggregates, and control (*i.e.*, no coating).

Compression and Flexural Tests

The compressive strength of concrete was determined by conducting cylinder load tests following ASTM C39.[49] Before testing, specimens were demolded, capped with sulfur mortar,[50] and placed in a water bath for 24 h. Specimens were then removed from the bath and mounted in an MTS load frame. Testing was done using a displacement-

Figure 5. A simply-supported beam specimen is mounted in an MTS load frame for four-point bending testing based on the guidelines specified in ASTM C78.

controlled rate of 0.51 mm/min (0.02 in/min), and this yielded an equivalent load rate that was within the range allowed as set forth in the ASTM guidelines.[49]

On the other hand, beam specimens were subjected to four-point bending tests for determining their flexural strength, otherwise known as the modulus of rupture. Following ASTM guidelines[51], the beam specimens were mounted in an MTS load frame as shown in Figure 5. Testing was performed using force-control and operated using a load rate of 8 kN/min. All of the cylinder and beam specimens were tested until failure, and during which, displacement and load data were recorded though the MTS data acquisition (DAQ) system interfaced with *LabVIEW*. Fracture patterns for each specimen were recorded and were compared to the fracture pattern figures provided in the ASTM guidelines for cylinder[49] and beam tests.[51]

Spatial Damage Detection Tests

Validation of spatial damage detection was performed using concrete plate specimens. Before testing, each plate was removed from its curing solution, rinsed with water, and then dried in a vacuum oven set to 75 °C for 24 h. Damage detection tests were performed on the plate specimens after they cooled down to room temperature, since their electrical resistance can be lower at elevated temperatures. First, in order to interrogate and collect the necessary data for EIT spatial conductivity mapping, a customized DAQ system was used. An Agilent 34980A multifunction switch with an embedded digital multimeter (DMM) formed the main unit of the DAQ system. A Keithley 6221 current source was also connected to the switch. Using a customized *MATLAB* software, the switch was commanded to

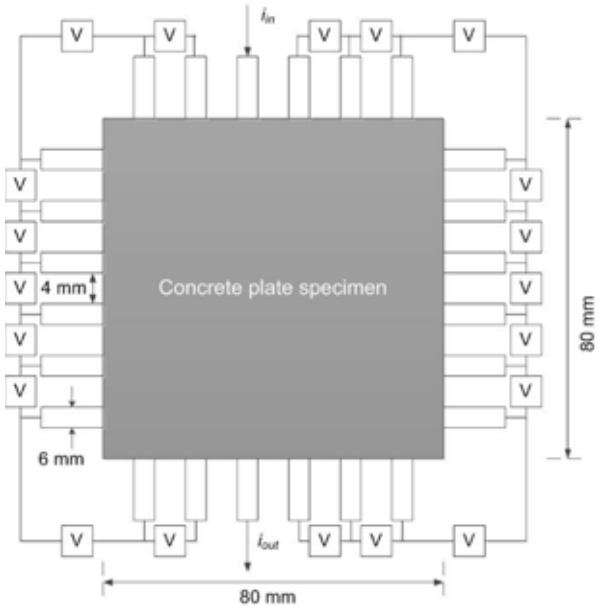

Figure 6. A schematic of a concrete plate instrumented with 24 boundary electrodes for EIT testing is shown. The EIT DAQ system injects electrical current across two opposite electrodes, while voltages are measured at all other remaining boundary electrodes.

interrogate the concrete plate specimens by injecting direct current (DC) across a pair of boundary electrodes, while the built-in DMM measured voltage at all other remaining boundary electrodes (Figure 6). This procedure was repeated so that current was injected across multiple pairs of boundary electrodes following an "across injection pattern" as defined by Loyola *et al.*[52]

Before damage was introduced to a specimen, a baseline EIT measurement of the undamaged specimen was obtained, using the aforementioned DAQ system and measurement strategy. Next, the specimens were subjected to localized damage by drilling 6.35 mm (0.25 in) holes, using a masonry drill bit, and at various locations in the plate. Drilling was done slowly to minimize excessive heating of the bit, since no coolant or lubricant was used. A total of three holes were drilled in each specimen. After drilling each hole, the DAQ system was employed for obtaining the corresponding EIT boundary voltage measurements.

Results and Discussion

Mechanical Properties

The compressive and flexural strength results are summarized in Tables 1 and 2. Here, values for compressive and flexural strengths are presented with the corresponding sample sets' w/c ratios and amount of SPL used during casting.

Table 1. Average compressive strengths of concrete cylinders.

Mix Design	w/c ratio	SPL [mL/kg]	Average compressive strength [psi]
Pristine (or untreated)	0.44	3.5	7,030
Aggregate-coated	0.44	3.5	6,500
Sand-coated	0.44	3.5	6,860
Sand- and aggregate-coated	0.44	3.5	7,580

Fracture patterns for all of the cylinders tested were type 1-3, following the diagrams given in ASTM C39[49], which means that the sulfur caps were level and provided uniform loading throughout the tests. From the results shown in Table 1, it can be seen that the lowest average compressive strength was for the aggregate-coated mix at 6,500 psi. Despite this, the compressive strength is well above the FAA guideline required strength of 4,400 psi.[46]. The sand-coated and both sand- and aggregate-coated sample sets exhibited average compressive strengths of 6,860 and 7,580 psi, respectively. On the other hand, the pristine specimens (*i.e.*, untreated or no thin film coating) had an average strength of 7,030 psi. From these results, it can be inferred that the mechanical properties of concrete can be maintained or even exceeded when cement-aggregate interfaces are modified with MWNT-latex thin films.

Overall, Table 1 suggests that sand-coated specimens could achieve the same, if not greater, compressive strengths as pristine concrete. However, coating the large aggregates degraded their inherent mechanical properties. While this can be perceived as a disadvantage of the approach of modifying the cement-aggregate interface with MWNT-latex thin films, the objective was to meet or exceed design guidelines (*i.e.*, 4,400 psi limit[46]) as opposed to deriving a technique that would not influence the material properties of concrete. Nevertheless, it was postulated that coating the aggregates diminished strength, since the MWNT-latex coating modified the chemistry and bonds that would have formed between the cement matrix and large aggregates. Coating the large aggregates could potentially create a smother surface that would reduce the effectiveness of bonding. Future studies will explore partial coatings on large aggregates as a compromise for enhancing electrical properties while mitigating the adverse impacts on compressive strength. In contrast, coating sand did not seem to produce adverse effects. This could be due to sands' smaller particle size and intrinsic jagged nature.

The beam tests and flexural strength results also provide a direct comparison on the differences in the mechanical properties of different sample sets, since they were casted using approximately the same w/c ratio and SPL content.

Table 2. Flexural strengths of concrete beam specimens.

Mix Design	w/c ratio	SPL [mL/kg]	Modulus of Rupture [psi]
Pristine	0.44	3.5	953
Aggregate-coated	0.42	3.5	950
Sand-coated	0.42	3.5	903
Sand- and aggregate-coated	0.43	3.5	821

All beam specimens fractured within the middle-third of the span, and based on ASTM C78, the modulus of rupture was calculated using equation (21):

$$R = \frac{PL}{bd^2} \tag{21}$$

where R is the modulus of rupture in [psi], P is the maximum applied load before failure in [lbf], L is the span length in [in], and b and d are the average width and depth of the specimen, respectively, at the failure plane and in [in]. Here, it can be shown that the average flexural strength of aggregate-coated beams was close to that of the pristine sample set. The sand-coated beam had a slight lower rupture modulus, but this value only differed by 6% as compared to the pristine specimen. Finally, the sample set with both types of aggregates coated with the films had a 14% flexural strength reduction. Despite this, these values are well above the minimum FAA requirements for rigid pavement design, which states that the modulus of rupture should give a minimum of 600 to 700 psi.[46]

Spatial Damage Detection Validation

In order to validate spatial damage detection using EIT, three different types of concrete plates were cast, each with dimensions of 80×80×20 mm^3. As mentioned earlier, six 6 mm-wide copper mesh electrodes, separated 4 mm apart, were embedded along each side of the square plates as shown in Figure 7. Damage was induced by drilling three holes at different locations in the plate.

First, damage detection tests were performed on pristine concrete plates (*i.e.*, concrete without any embedded CNT thin films), and the test specimen and corresponding EIT results are shown in Figure 7. As with all tests, the EIT DAQ system was employed for measuring the boundary voltages before and after the introduction of damage. It can be seen from the reconstructed resistivity distributions of the concrete plates (Figures 7e to 7h) that no apparent changes in

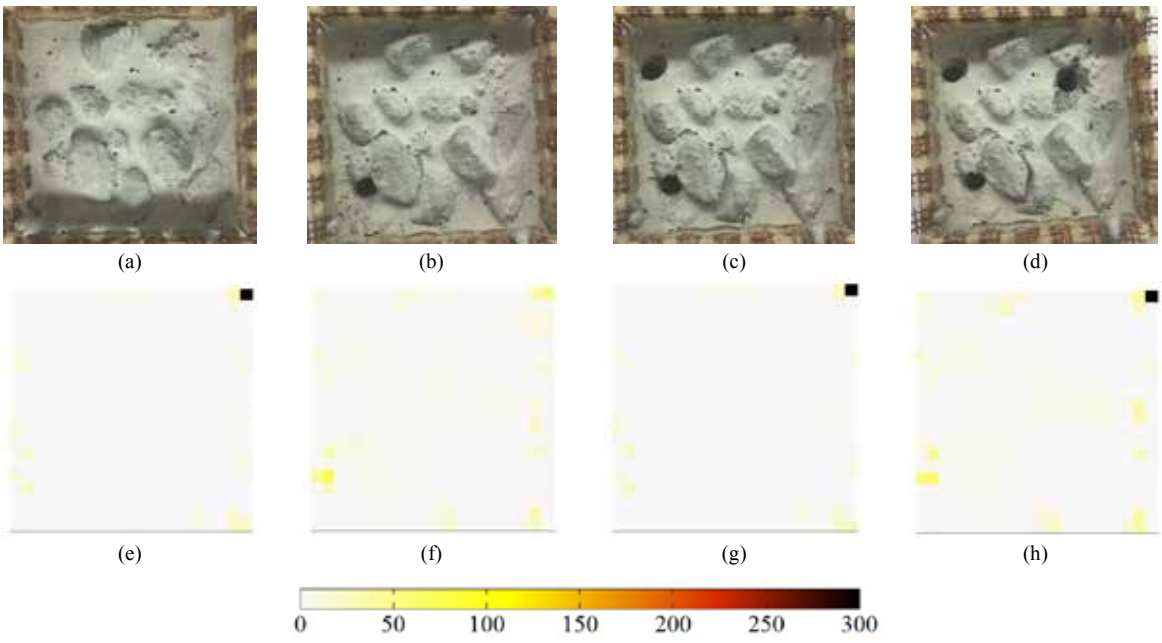

Figure 7. Damage detection tests were performed on (a) pristine concrete plates. Holes were drilled near the (b) bottom-left, (c) top-left, and then (d) top-right corners of the plate. (e) The spatial resistivity distribution of the undamaged plate is shown. The change in resistivity distribution was also calculated with respect to the undamaged baseline after the introduction of drilled-hole damage near the (f) bottom-left, (g) top-left, and (h) top-right corners.

resistivity distributions were observed due to damage. The application of EIT on its own on concrete did not enable damage detection. A reason for this could be the fact that the resistivity of pristine concrete is too high. Hence, applied electrical current could not sufficiently propagate through the entire material (*i.e.*, electrical current only flowed through the path of least resistance), and the measured boundary voltage responses were not sensitive to damage features created by drilling holes. The same testing procedure was also repeated for concrete casted using large aggregates coated with MWNT-latex thin films, and a set of representative results are shown in Figure 8. Similarly, spatial damage detection was unsuccessful for the same reasons mentioned previously. It was hypothesized that coating the large aggregates alone did not create sufficient amounts of conductive interfaces for electrical current to propagate effectively throughout the entire plate. As a result, a percolation (or near-percolation) system was not formed, and applied electrical current did not generate boundary voltage responses that were sensitive to damage.

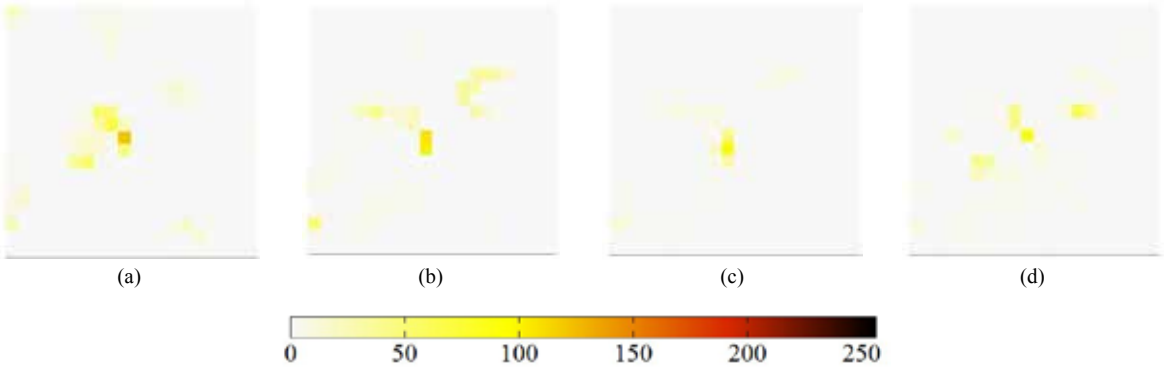

Figure 8. Damage detection tests were performed on aggregate-coated concrete plates. The spatial resistivity map for the (a) undamaged and the change in spatial resistivity distribution corresponding to a hole drilled near the (b) bottom-left, (c) top-left, and (d) top-right did not successfully detect damage.

In contrast, sand-coated and both sand- and aggregate-coated concrete plates, when coupled with the EIT algorithm, yielded drastically different results, as shown in Figures 9 and 10, respectively. For these two sample sets, electrical current applied across two opposite electrodes was able to propagate throughout the entire plate, and the EIT spatial

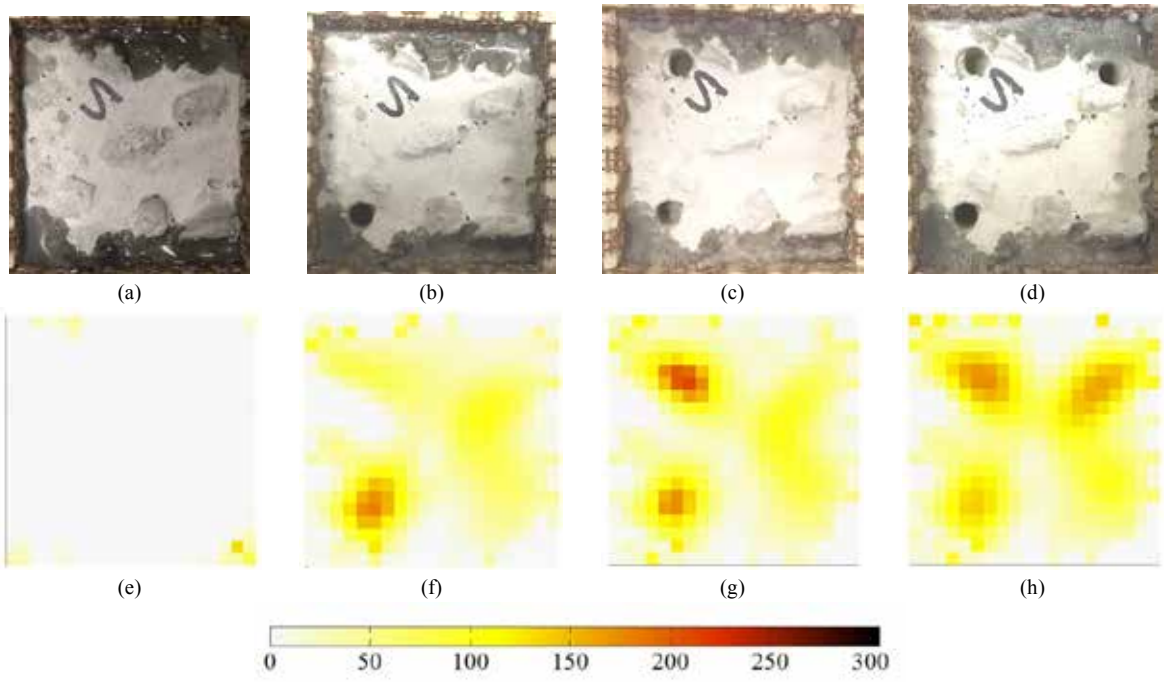

Figure 9. Damage detection tests were performed on (a) concrete plates cast using sand coated with MWNT-latex thin films. Holes were drilled near the (b) bottom-left, (c) top-left, and then (d) top-right corners of the plate. (e) The spatial resistivity distribution of the undamaged specimen is shown. The change in resistivity distribution was also calculated with respect to the undamaged baseline after the introduction of drilled-hole damage near the (f) bottom-left, (g) top-left, and (h) top-right corners.

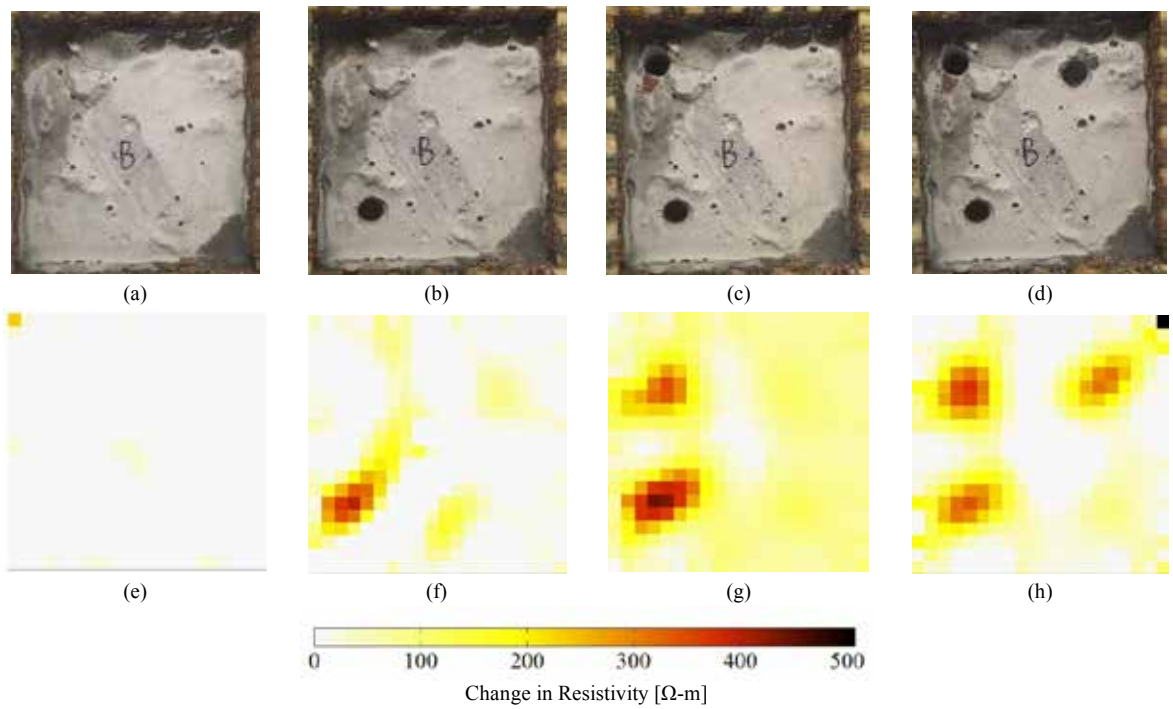

Figure 10. Damage detection tests were performed on (a) concrete plates cast using sand and large aggregates coated with MWNT-latex thin films. Holes were drilled near the (b) bottom-left, (c) top-left, and then (d) top-right corners of the plate. (e) The spatial resistivity distribution of the undamaged specimen is shown. The change in resistivity distribution was also calculated with respect to the undamaged baseline after the introduction of drilled-hole damage near the (f) bottom-left, (g) top-left, and (h) top-right corners.

resistivity maps clearly show localized increases in resistivity that coincided with the locations of drilled holes. When comparing the results shown in Figures 9 and 10, it can be seen that the signal-to-noise ratio is higher (*i.e.*, the magnitude of the change in resistivity is larger) for concrete casted using both sand and aggregates coated with the MWNT-latex thin films. This result was observed because these specimens were characterized by higher electrical conductivity due to the presence of more conductive cement-aggregate interfaces. In short, spatial damage detection is only possible when current can propagate through the entire body, and its path is perturbed significantly by damage (or localized resistivity or conductivity changes) so that boundary voltage changes can be observed. Otherwise, EIT cannot detect changes in resistivity from inverse analysis, as can be seen from the results shown in Figures 7 and 8.

Cost Analysis

A simple cost analysis was performed to compare the proposed technique of modifying cement-aggregate interfaces using MWNT-latex thin films versus the current state-of-art of directly dispersing carbon nanotubes in the cement matrix. Table 3 shows a summary of the increase in estimated costs (in U.S. dollars) of MWNTs required assuming

Table 3. Cost matrix comparing additional costs of incorporating carbon nanotubes in concrete.

Unit price	MWNT content	Additional cost
MWNT: $5,000 / kg	0.5 *wt.*%	$6,400
	0.1 *wt.*%	$1,280
	0.05 *wt.*%	$640
	0.034 *wt.*% (sand-coated)	$435
	0.025 *wt.*% (aggregate-coated)	$320

Note: All prices are shown in U.S. dollars.

that 256 kg of cementitious content is needed for 1 m^3 of concrete (based on FAA guidelines).[46] All weight percentage concentrations of carbon nanotubes are with respect to the amount of cement or cementitious material used in the mix design. The larger weight percentages are comparable to the quantities used by Yu and Kwon.[11] The last two rows correspond to concrete specimens presented in this work, and MWNT concentrations were calculated based on the total weight of nanotubes used during ink preparation and spray fabrication (*i.e.*, material lost during spray coating was accounted for in these calculations and represents opportunities for futher lowering the cost of this technique).

Given that the average price of concrete is ~US$122 per cubic meter[53], significant increases in costs can be observed if CNTs are directly dispersed in the cement matrix. For instance, concrete containing 0.5 *wt.*% of MWNTs would incur 52 times additional costs as compared to pristine concrete. In comparison, sand-coated specimens in this study would incur dramatically less increases in cost (Table 3). The lower cost of modifying cement-aggregate interfaces makes this an attractive technique for real-world, practical implementations of this material. It should be noted that the specimens casted in this study have not been optimized for sensing and mechanical performance, and further reductions in cost are possible and will be reserved for future studies.

Conclusions

In this study, a new method for casting multifunctional cementitious composites was presented and was based on altering cement-aggregate interfaces. Fine and coarse aggregates were pre-coated with a highly conductive MWNT-latex thin film that was deposited using airbrushing or spray coating. In doing so, CNTs remained dispersed within the films, which could then be uniformly dispersed throughout concrete along with the aggregates. A direct result is dramatic reductions in the amount of nanotubes used during casting and associated costs while still providing enough

conductive material for establishing a conductive network within the bulk material for damage detection purposes. In addition, the proposed technique does not modify existing mix designs nor construction practices.

Four unique concrete sample sets were cast; they were the control (pristine or untreated concrete) and concrete cast using MWNT-latex thin films coated onto sand, large aggregates, and both sand and large aggregates. Compression and bending tests were conducted on cylinder and beam specimens, respectively, for assessing their mechanical properties. First, all of the specimens exceeded the minimum strength requirements as set forth by FAA rigid concrete pavement design guidelines. Second, the sand-coated and aggregate-coated sample sets exhibited comparable flexural strengths as compared to the control, whereas the sand-coated and sand- and large aggregate-coated sample sets were characterized by similar, if not higher, compressive strengths versus the control. Then, using concrete plate specimens coupled with an EIT algorithm, spatial damage detection tests were conducted. The results showed that the sand-coated and both sand- and aggregate-coated concrete sample sets enabled damage detection, due to the fact that electrical current was able to propagate throughout the entire bulk material. EIT was able to map the spatial resistivity distributions of plate specimens, and damage (in the form of drilled holes) were successfully detected as highly localized resistivity changes that coincided with the locations of those holes. In contrast, EIT was unable to detect damage in untreated concrete and large aggregate-coated specimens. In general, spatial damage detection is only possible if applied electrical current could propagate throughout the entire material so as to generate boundary voltage responses that are sensitive to damage.

Acknowledgments

This research was funded by the U.S. Federal Aviation Administration (FAA) under cooperative agreement no. 13-G-017 and was also partially supported by the U.S. National Science Foundation (NSF) under grant no. CMMI-1200521. The authors would like to express their sincerest gratitude to the collaborators on this project, Dr. Navneet Garg (FAA), Dr. Rongzong Wu (University of California, Davis) and Prof. Jerome Lynch (University of Michigan), for their immense support throughout various phases of this project.

References

1. Saafi M. Wireless and Embedded Carbon Nanotube Networks for Damage Detection in Concrete Structures. *Nanotechnology*. 2009; 20(395502): 1-7.
2. Song G, Gu H and Mo Y-L. Smart Aggregates: Multi-Functional Sensors for Concrete Structures—a Tutorial and a Review. *Smart Materials and Structures*. 2008; 17(033001): 1-17.
3. Banthia N, Djeridane S and Pigeon M. Electrical Resistivity of Carbon and Steel Micro-Fiber Reinforced Cements. *Cement and Concrete Research*. 1992; 22: 804-14.
4. Banthia N and Sheng J. Micro-Reinforced Cementitious Materials. In: *MRS Proceedings*, 1990, pp. 25-32.
5. Ding Y, Han Z, Zhang Y and Azevedo CM. Hybrid Use of Steel and Carbon-Fiber Reinforced Concrete for Monitoring of Crack Behavior. In: *ECCM15–15th European Conference on Composite Materials*, Venice, Italy, 2012 June 24-28, pp. 1-8.
6. Chen P-W and Chung D. Carbon Fiber Reinforced Concrete as an Intrinsically Smart Concrete for Damage Assessment During Static and Dynamic Loading. *ACI materials Journal*. 1996; 93: 341-50.
7. Fu X, Lu W and Chung D. Improving the Strain-Sensing Ability of Carbon Fiber-Reinforced Cement by Ozone Treatment of the Fibers. *Cement and Concrete Research*. 1998; 28: 183-7.
8. Ma P-C, Siddiqui NA, Marom G and Kim J-K. Dispersion and Functionalization of Carbon Nanotubes for Polymer-Based Nanocomposites: A Review. *Composites Part A: Applied Science and Manufacturing*. 2010; 41: 1345-67.
9. Salvetat J-P, Bonard J-M, Thomson N, et al. Mechanical Properties of Carbon Nanotubes. *Applied Physics A*. 1999; 69: 255-60.
10. Wei B, Vajtai R and Ajayan P. Reliability and Current Carrying Capacity of Carbon Nanotubes. *Applied Physics Letters*. 2001; 79: 1172-4.
11. Yu X and Kwon E. A Carbon Nanotube/Cement Composite with Piezoresistive Properties. *Smart Materials and Structures*. 2009; 18(055010): 1-5.
12. Loh KJ and Gonzalez J. Cementitious Composites Engineered with Embedded Carbon Nanotube Thin Films for Enhanced Sensing Performance. In: *Journal of Physics: Conference Series*, pp. 1-8.
13. Wang H, Zhou W, Ho DL, et al. Dispersing Single-Walled Carbon Nanotubes with Surfactants: A Small Angle Neutron Scattering Study. *Nano Letters*. 2004; 4: 1789-93.
14. Lin VW, Li M, Lynch JP and Li VC. Mechanical and Electrical Characterization of Self-Sensing Carbon Black Ecc. In: *SPIE Smart Structures and Materials+ Nondestructive Evaluation and Health Monitoring*, San Diego,CA, 2011 March 6, pp. 1-12.
15. Khoury S, Aliabdo AA-H and Ghazy A. Reliability of Core Test–Critical Assessment and Proposed New Approach. *Alexandria Engineering Journal*. 2014; 53: 169-84.
16. Han B, Yu Y, Han B and Ou J. Development of a Wireless Stress/Strain Measurement System Integrated with Pressure-Sensitive Nickel Powder-Filled Cement-Based Sensors. *Sensors and Actuators A: Physical*. 2008; 147: 536-43.
17. Ding Y, Chen Z, Han Z, Zhang Y and Pacheco-Torgal F. Nano-Carbon Black and Carbon Fiber as Conductive Materials for the Diagnosing of the Damage of Concrete Beam. *Construction and Building Materials*. 2013; 43: 233-41.
18. Mortensen LP, Ryu DH, Zhao YJ and Loh KJ. Rapid Assembly of Multifunctional Thin Film Sensors for Wind Turbine Blade Monitoring. *Key Engineering Materials Journal*. 2013; 569: 515-22.
19. Holder DS. *Electrical Impedance Tomography: Methods, History and Applications*. CRC Press, 2004.
20. Barber D. Quantification in Impedance Imaging. *Clinical Physics and Physiological Measurement*. 1990; 11: 45-56.
21. Dijkstra A, Brown B, Leathard A, Harris N, Barber D and Edbrooke D. Review Clinical Applications of Electrical Impedance Tomography. *Journal of Medical Engineering & Technology*. 1993; 17: 89-98.
22. Smallwood R, Mangnall Y and Leathard A. Transport of Gastric Contents (Electric Impedance Imaging). *Physiological Measurement*. 1994; 15: A175-88.
23. Brown B, Barber D, Eyüboglu B, Harris N and McArdle F. Electrical Impedance Imaging Developed to Image Cardiopulmonary Function. In: *Proc 9th Int Conf IEEE Eng Med Biol Society*, Boston,MA,, 1987 Nov 1, pp. 1200-2.
24. Brown B, Sinton A, Barber D, Leathard A and McArdle F. Simultaneous Display of Lung Ventilation and Perfusion on a Real-Time EIT System. In: *Engineering in Medicine and Biology Society, 14th Annual International Conference of the IEEE*, Paris,France, 1992 Oct 9, pp. 1710-1.
25. Goharian M. New Hardware and Software Design for Electrical Impedance Tomography. 2007.
26. Harris N, Brown B and Barber D. Continuous Monitoring of Lung Ventilation with Electrical Impedance Tomography. In: *Engineering in Medicine and Biology Society, 1992 14th Annual International Conference of the IEEE*, Paris,France, 1992 Oct 29, pp. 1754-5.
27. Murphy D, Burton P, Coombs R, Tarassenko L and Rolfe P. Impedance Imaging in the Newborn. *Clinical Physics and Physiological Measurement*. 1987; 8: 131-40.
28. Newell JC, Edic PM, Ren X, Larson-Wiseman JL and Danyleiko MD. Assessment of Acute Pulmonary Edema in Dogs by Electrical Impedance Imaging. *Biomedical Engineering, IEEE Transactions on*. 1996; 43: 133-8.
29. Loh KJ, Hou T-C, Lynch JP and Kotov NA. Carbon Nanotube Sensing Skins for Spatial Strain and Impact Damage Identification. *Journal of Nondestructive Evaluation*. 2009; 28: 9-25.
30. Loyola BR, Briggs TM, Arronche L, et al. Detection of Spatially Distributed Damage in Fiber-Reinforced Polymer Composites. *Structural Health Monitoring*. 2013; 12: 225-39.
31. Loyola BR, Saponara V, Loh KJ, Briggs TM, O'Bryan G and Skinner JL. Spatial Sensing Using Electrical Impedance Tomography. *Sensors Journal, IEEE*. 2013; 13: 2357-67.
32. Zhang D, Ye L, Wang D, Tang Y, Mustapha S and Chen Y. Assessment of Transverse Impact Damage in GF/EP Laminates of Conductive Nanoparticles Using Electrical Resistivity Tomography. *Composites Part A: Applied Science and Manufacturing*. 2012; 43: 1587-98.
33. Tallman T, Gungor S, Wang K and Bakis C. Damage Detection and Conductivity Evolution in Carbon Nanofiber Epoxy Via Electrical Impedance Tomography. *Smart Materials and Structures*. 2014; 23(045034): 1-9.
34. Hallaji M, Seppänen A and Pour-Ghaz M. Electrical Impedance Tomography-Based Sensing Skin for Quantitative Imaging of Damage in Concrete. *Smart Materials and Structures*. 2014; 23(085001): 1-13.
35. Hou T-C and Lynch JP. Tomographic Imaging of Crack Damage in Cementitious Structural Components. In: *4th International Conference on Earthquake Engineering*, Taipei,Taiwan, 2006 Oct 12-13, pp. 12-3.
36. Hou T-C and Lynch JP. Electrical Impedance Tomographic Methods for Sensing Strain Fields and Crack Damage in Cementitious Structures. *Journal of Intelligent Material Systems and Structures*. 2008: 1-18.

37. Gupta S, Gonzalez J and Loh K. Damage Detection Using Smart Concrete Engineered with Nanocomposite Cement-Aggregate Interfaces. In: *10th International Workshop on Structural Health Monitoring* Stanford,CA, 2015 Sep 1-3, pp. 3033-41.
38. Sherina ES and Starchenko AV. Finite Volume Schemes for the Electrical Impedance Tomography Problem. *Vestnik Tomskogo Gosudarstvennogo Universiteta Matematika i Mekhanika*. 2014: 25-38.
39. Lazarovitch R, Rittel D and Bucher I. Experimental Crack Identification Using Electrical Impedance Tomography. *NDT & E International*. 2002; 35: 301-16.
40. Polydorides N. Image Reconstruction Algorithms for Soft-Field Tomography. University of Manchester: UMIST, 2002
41. Soleimani M. Image and Shape Reconstruction Methods in Magnetic Induction and Electrical Impedance Tomography. Citeseer, 2005
42. Vauhkonen M. Electric Resistance Tomography and Prior Information PhD. Thesis, Kuopio University, Finland, 1997
43. Cheng K-S, Isaacson D, Newell J and Gisser DG. Electrode Models for Electric Current Computed Tomography. *Biomedical Engineering, IEEE Transactions on*. 1989; 36: 918-24.
44. Fish J and Belytschko T. *A First Course in Finite Elements*. John Wiley & Sons, 2007.
45. Hughes TJ. *The Finite Element Method: Linear Static and Dynamic Finite Element Analysis*. Courier Corporation, 2012.
46. Standards for Specifying Construction of Airports. *AC 150/5370-10G*. Federal Aviation Administration, 2014.
47. Wang L and Loh KJ. Spray-coated Carbon Nanotube-Latex Strain Sensors. *Science Letter Journal*. 2016; 5(234): 1-10.
48. ASTM C31/C31M - 15 : Standard Practice for Making and Curing Concrete Test Specimens in the Field. West Conshohocken, Pa: ASTM International, 2015.
49. ASTM C39/C39M - 15a : Standard Test Method for Compressive Strength of Cylindrical Concrete Specimens. West Conshohocken, Pa: ASTM International, 2015.
50. ASTM C617/C617M - 15 : Standard Practice for Capping Cylindrical Concrete Specimens. West Conshohocken, Pa: ASTM International, 2015.
51. ASTM C78/C78M - 15a : Standard Test Method for Flexural Strength of Concrete (Using Simple Beam with Third-Point Loading). West Conshohocken, Pa: ASTM International, 2015.
52. Loyola BR. Distributed in Situ Health Monitoring of Conductive Self-Sensing Fiber-Reinforced Polymers Using Electrical Impedance Tomography. PhD Thesis, University of California,Davis, 2012
53. Corydon LF. Ready Mixed Concrete Industry Data Report. National Ready Mixed Concrete Association, 2012.